Subscriber access provided by KU Leuven University Library

Article

Arrays of pentacene single crystals by stencil evaporation

Pavlo Fesenko, Valentin Flauraud, Shenqi Xie, Juergen
Brugger, Jan Genoe, Paul Heremans, and Cedric Rolin

Cryst. Growth Des., **Just Accepted Manuscript** • DOI: 10.1021/acs.cgd.6b00765 • Publication Date (Web): 24 Jun 2016

Downloaded from http://pubs.acs.org on July 5, 2016

Just Accepted

"Just Accepted" manuscripts have been peer-reviewed and accepted for publication. They are posted online prior to technical editing, formatting for publication and author proofing. The American Chemical Society provides "Just Accepted" as a free service to the research community to expedite the dissemination of scientific material as soon as possible after acceptance. "Just Accepted" manuscripts appear in full in PDF format accompanied by an HTML abstract. "Just Accepted" manuscripts have been fully peer reviewed, but should not be considered the official version of record. They are accessible to all readers and citable by the Digital Object Identifier (DOI®). "Just Accepted" is an optional service offered to authors. Therefore, the "Just Accepted" Web site may not include all articles that will be published in the journal. After a manuscript is technically edited and formatted, it will be removed from the "Just Accepted" Web site and published as an ASAP article. Note that technical editing may introduce minor changes to the manuscript text and/or graphics which could affect content, and all legal disclaimers and ethical guidelines that apply to the journal pertain. ACS cannot be held responsible for errors or consequences arising from the use of information contained in these "Just Accepted" manuscripts.

Crystal Growth & Design is published by the American Chemical Society. 1155 Sixteenth Street N.W., Washington, DC 20036
Published by American Chemical Society. Copyright © American Chemical Society. However, no copyright claim is made to original U.S. Government works, or works produced by employees of any Commonwealth realm Crown government in the course of their duties.

Arrays of pentacene single crystals by stencil evaporation

Pavlo Fesenko[1,2*], *Valentin Flauraud*[3], *Shenqi Xie*[3], *Jürgen Brugger*[3], *Jan Genoe*[1,2], *Paul Heremans*[1,2], *Cédric Rolin*[1]

[1] imec, Large Area Electronics, Kapeldreef 75, 3001 Leuven, Belgium

[2] KU Leuven, Department of Electrical Engineering, Kasteelpark Arenberg 10, 3001, Leuven, Belgium

[3] EPFL, Microsystems Laboratory 1, Station 17, CH-1015 Lausanne, Switzerland

[*]Corresponding author. Tel.: +32 16 28 33 53. E-mail address: pavlo.fesenko@imec.be

Keywords: organic semiconductors, pentacene, single crystals, stencil evaporation, diffusion.

Abstract

In order to realize high-performance organic thin-film transistors (TFT), two parameters of the organic semiconducting layer are desired: single crystallinity for high mobility, and patterning for low off currents. High-quality single crystals can be fabricated using vapor techniques such as physical vapor transport (PVT) but they require high temperatures close to thermodynamic equilibrium, for example, 240°C for pentacene. Such high temperatures are not ideal for TFT fabrication on plastic substrates and limit the use of PVT in flexible electronics applications.

In this work arrays of pentacene single crystals were directly deposited at low temperature of 40°C by vacuum thermal evaporation through micro-fabricated stencil masks (stencil lithography). By decreasing the stencil aperture size down to 1 μm x 1 μm, we were able to limit the nucleation area until only one grain per aperture is nucleated and grown. We studied systematically scaling effects for large singe crystal growth and discuss details of the growth morphology. We found for instance that the formed pentacene crystals are one monolayer thick and the crystal area is much larger than the aperture size. This can be explained by the diffusion of adsorbed molecules on the surface laterally under the shadow mask, where they are protected from other impinging molecules. The diffusion away from the impinging area under the aperture affects the nucleation density inside this area and was used to calculate the diffusion length to nucleation $\lambda_N = 0.66 \pm 0.11$ μm of pentacene on SiO_2 at 40°C. Our diffusion-driven growth of organic single crystals by stencil lithography is a direct method to grow patterned arrays of single crystalline organic thin-film semiconductor layers.

Introduction

Organic semiconductors are promising candidates for the fabrication of thin-film transistors (TFT) on large-area flexible substrates because they can be processed at low temperature[1,2] and potentially at low cost.[3,4] TFT performance improves significantly upon a minimization of the number of grain boundaries in organic thin films as these boundaries act as energy barriers for percolating charges.[5–7] Additionally, the patterning of the semiconductor film is required to achieve low off currents in electrical devices.[8] As a result, the growth of high-density arrays of organic single crystals is a desirable semiconductor film topology to achieve arrays of high-performance organic TFTs that can be exploited in large-area flexible circuits such as display backplanes.[9–12]

Among different film deposition techniques, evaporation provides high material purity along with controlled thickness and uniformity over large areas.[3] The vapor phase growth of single organic crystals is traditionally performed by physical vapor transport (PVT) in process conditions close to thermodynamics equilibrium.[13] The growth of arrays of single pentacene crystals by PVT has been previously achieved using substrates with patterned self-assembled monolayers (SAM).[9] The nucleation of pentacene molecules was localized to the rough SAM films and resulted in growth of single crystals on areas of 5 µm x 5 µm. The main disadvantages of this method, however, are the high substrate temperature (≈ 240°C for pentacene), very limited control over film thickness, long processing times and difficult up scaling of the PVT technology.

In this work, we demonstrate how arrays of pentacene single crystals can be formed on a SiO_2 substrate using traditional vacuum thermal evaporation (VTE) and micro-fabricated reusable shadow masks (stencils) applied on the substrate for patterning. The pentacene evaporation is performed at low substrate temperatures (40°C), moderate deposition rates (0.1 Å/s) and precise control over film thickness is achieved. During evaporation through stencil masks with micron scale apertures, individual nucleation events take place on the surface area under each aperture, resulting, upon further growth, in the formation of well-localized single crystals. In conjunction with photolithographic device fabrication techniques, this simple and up-scalable method[14] has the potential to deliver high density arrays of organic single crystal TFTs.

Results

To realize stencil evaporation, a silicon nitride shadow mask with micro-fabricated apertures is applied on the substrate and the assembly is then mounted into the VTE chamber where the organic semiconductor is evaporated in standard conditions. In order to study the impact of stencil aperture geometry on film morphology, we evaporated pentacene on a SiO_2 substrate through a stencil mask with square apertures of side dimensions a = 10 μm and a = 1 μm shown by scanning electron microscopy (SEM) in Figs. 1a and 1d, respectively. Pentacene evaporation was performed at a deposition rate r_{dep} = 0.1 Å/s and at a substrate temperature T = 40°C. The nominal film thickness was monitored using a quartz crystal monitor calibrated for pentacene growth in absence of the stencil mask.

First, we evaporated submonolayer films with a nominal thickness of 0.6 nm to investigate the nucleation and initial growth of pentacene grains. In the case of large apertures (a = 10 μm), the SEM image in Fig. 1b shows multiple grains per aperture. This layer morphology resembles that of pentacene submonolayers grown in the absence of a stencil mask. Closer inspection of Fig. 1b reveals, however, that the grain density on the edges of the square is lower than in the center. In small apertures (a = 1 μm), the SEM image of Fig. 1e shows that only single grains are present in each aperture. A few small grains are also present outside of the areas exposed by the apertures.

We attribute these to heterogeneous nucleation on surface inhomogeneities. On the other hand, the larger grains observed inside exposed areas are attributed to homogeneous nucleation.

Next, we used the same conditions to evaporate thicker pentacene films with a nominal thickness of 20 nm. The atomic force microscopy (AFM) image in Fig. 1c shows that growth through large apertures results in dendritic and terraced islands with an average thickness close to the nominal thickness. This morphology corresponds to what is typically observed for pentacene films in the absence of stencil masks.[15] On the other hand, the growth through small apertures yield a completely different morphology. The AFM image in Fig. 1f reveals oval islands with a thickness of 1.5 nm corresponding to a single monolayer of pentacene. A direct comparison of Figs. 1d and 1f show that the lateral island dimensions extend well beyond the aperture area by several µm.

Figure 1. Scanning electron microscopy (SEM) images of the stencil apertures of a) a = 10 µm, d) a = 1 µm. SEM images of 0.6 nm thick pentacene submonolayer films evaporated through the apertures of b) a = 10 µm, e) a = 1 µm. Borders of the apertures are marked with white dashed squares. Atomic force microscopy (AFM) images of pentacene films with nominal evaporated thickness of 20 nm, evaporated through the apertures of c) a = 10 µm, f) a = 1 µm. The height profiles along the white lines are shown in the inset: The measured thickness is 20 nm in Fig. 1c and 1.5 nm in Fig. 1f. The scale bars on all images are 5 µm.

To assess the crystallinity of the monolayer islands grown through the small apertures in Fig. 1f, we applied two techniques: transverse shear microscopy (TSM) (Fig. 2a) and differential interference contrast (DIC) (Fig. 2b). TSM is a contact-mode AFM technique that probes elastic anisotropy of thin films.[16] From the intensity of the TSM signal, different in-plane crystal orientations can be assigned to the pentacene islands. DIC is an optical technique that can probe optical anisotropy of thin films.[17] As shown in Fig. 2c, fast and slow axes n_1, n_2 obtained from the DIC signal correspond to the crystallographic axes *b* and *a*, respectively.[18] The uniform TSM and DIC brightness of each monolayer island demonstrates their single crystalline nature. In addition, all monolayer islands have a distinctive elliptical shape that correlates with their orientation. As shown in Fig. 2a, the long and short elliptical axes respectively correspond to crystallographic axes *a* and *b*. Since crystal growth proceeds at different speeds along different axes, the elliptical shape of each island reflects the equilibrium crystal shape, or crystal habit, of pentacene (white octagon in Fig. 2a).[19]

Figure 2. a) Transverse shear microscopy (TSM) and b) differential interference contrast (DIC) images of 1.5 nm thick pentacene film evaporated through the apertures of a = 1 µm. The equilibrium crystal shape of pentacene (white octagon) and the crystallographic axes *a*, *b* are shown in (a). The fast and slow axes n_1, n_2 of the islands in (b) are assigned according to the DIC brightness. Using c) the relationship between molecular structure and optical properties of pentacene thin films, the crystallographic axes *a*, *b* of the islands can be deduced from the orientation of the fast and slow axes n_1, n_2 in (b). The scale bars on all images are 5 µm.

Besides stencil aperture size *a*, the distance between apertures *d* also profoundly affects growth morphology. So far *d* has been kept relatively large at *d* = 5 µm where little cross talk between neighboring apertures is observed (first row in Fig. 3). The second row in Fig. 3 shows the effect of decreasing aperture distance down to *d* = 1 µm. For the largest aperture *a* = 10 µm, a variation in *d* has no effect on film morphology (compare Figs. 3c and 3f). On the other hand, for *a* = 1 µm, the elliptical islands observed in Fig. 3b are no longer present. Instead, the film morphology combines two-dimensional crystallites encompassing several apertures and square-shaped three-dimensional crystallites located in about half of the apertures. When stepping to the smallest apertures *a* = 0.5 µm, at large *d* in Fig. 3a, the evaporation of the 20 nm nominal pentacene film leaves very little material behind: homogeneous nucleation is suppressed in all apertures and only a few randomly distributed grains resulting from heterogeneous nucleation are observed. Upon decreasing *d*, however, a submonolayer film is obtained in Fig. 3d with monolayer grains encompassing several apertures. Clearly, at sufficiently low *a* and *d*, a cross-talk between neighboring apertures affects the film morphology.

Figure 3. AFM images of 20 nm thick pentacene film for aperture sizes a), d) *a* = 10 µm, b), e) *a* = 1 µm, c), f) *a* = 0.5 µm. The pitch between apertures is a), b), c) *d* = 5 µm and d), e), f) *d* = 1 µm. The scale bars on all images are 5 µm.

Discussion

Due to the natural bow and waviness of the stencil mask and the substrate, a few µm gap exists between the substrate and the stencil as schematically shown in Fig. 4. After a ballistic travel through the vacuum chamber and through the stencil apertures, evaporated organic molecules are adsorbed on the substrate surface and form a thermalized 2D molecular gas.[20,21] Adsorbed molecules can have four fates: They can desorb; they can participate in the nucleation of a new cluster if critical supersaturation to nucleation $\Delta\mu_{\mathrm{cr}}$ is locally reached; they can aggregate on a growing stable cluster; they can diffuse away from the aperture area and eventually desorb.

The surface diffusion of adsorbed molecules away from the aperture area is of special importance in stencil evaporation. This diffusion lowers the surface concentration of individual molecules n_1 along the aperture edges, resulting in a n_1 profile with smeared edges that is mathematically defined by a negative exponential (dotted line in Fig. 4). In the boundary region affected by diffusion, local supersaturation and, consequently, nucleation probability are lower than in the central unaffected region. In the central region, characterized by the plateau of the n_1 profile, growth remains unaffected by the presence of the stencil mask and multiple nucleation events occur simultaneously. Upon decreasing aperture size a, the surface of the plateau progressively shrinks until the whole aperture area is affected by diffusion. In this case, the n_1 profile becomes a peak with a maximum concentration in the center of the aperture. This situation is favorable to a single nucleation event in each aperture, as $\Delta\mu_{\mathrm{cr}}$ is sooner reached in the center of the aperture. Finally, further decrease of a can completely suppress nucleation (as in Fig. 3a) when the build up in n_1 is insufficient to reach $\Delta\mu_{\mathrm{cr}}$.

Figure 4. Schematics of the stencil evaporation. The substrate is exposed to the deposition flux R of organic molecules through micro-fabricated stencil apertures. Diffusion of adsorbed

molecules away from the aperture area decreases their surface concentration n_1 along the aperture edges affecting nucleation and growth in the boundary region.

In order to formalize the description above, we conducted a submonolayer growth of pentacene using a stencil with aperture sizes a = 0.5, 1, 2, 5 and 10 μm. For each a, we extracted the average nucleation density $\overline{N}$ by counting the total number of grains inside the aperture and dividing it by a^2. Statistics for $\overline{N}$ were acquired from three different areas of 25 μm x 15 μm that include several apertures of the same size. This data is shown in Fig. 5a. The asymptotic point at a = 100 μm shows the nucleation density in the absence of stencil $N_0 = 1.83 \pm 0.01$ μm^{-2} (see Fig. S2 in the Supporting Information for the extraction of N_0). Upon decreasing a, $\overline{N}$ drops below N_0 due to diffusive losses at the edges of the aperture. At a = 0.5 μm almost no nucleation was observed.

Figure 5. a) Average nucleation density $\overline{N}$ of pentacene islands as a function of the aperture size a. The points represent the experimental values for the substrate temperature of 40°C and the deposition rate of 0.1 Å/s. The solid lines are fitted curves using a single parameter λ_N. The dashed line is the nucleation density unaffected by diffusion losses N_0. b) Simulated nucleation density $N(x, y)$ for a = 10 μm. The simulation parameters are $D = 1$ μm^2/s, $\tau_N = 0.25$ s that correspond to $\lambda_N = 0.5$ μm. The molecular diffusion flux is marked by red arrows. The scale bar is 5 μm.

To understand how $\overline{N}$ depends on a in Fig. 5a, we propose a numerical model that predicts $\overline{N}$ based on the concentration of adsorbed single molecules n_1. It consists of several steps: 1) Find $n_1(x, y, t)$ by solving the time-dependent diffusion equation, 2) Calculate the local deposition flux $R(x, y)$ by taking the time derivative of n_1, 3) Calculate the local nucleation density $N(x, y)$ from $R(x, y)$, and 4) Calculate $\overline{N}$ by integrating $N(x, y)$. The time-dependent diffusion equation gives a macroscopic description of $n_1(x, y, t)$:[22]

$$\frac{\partial n_1(x,y,t)}{\partial t} = D\Delta n_1(x,y,t) + R_0(x,y) \tag{1}$$

where D is the diffusion coefficient of molecular adsorbates on the substrate and $R_0(x, y)$ is the nominal deposition flux. In the case of stencil evaporation, $R_0(x, y)$ is a piecewise function that is equal to R_0 in the aperture area and zero everywhere else. The desorption term is neglected because pentacene molecules are in the complete condensation regime at the substrate temperature of 40°C.[23] Equation (1) is limited to the description of the early stage of growth before nucleation of stable clusters. At this stage, the surface diffusion of adsorbed molecules is characterized by a diffusion length $\lambda_D = \sqrt{Dt}$ that represents the average travel distance of adsorbed molecules at time t. In the early stage and complete condensation regime considered here, the event that limits molecular diffusion is nucleation. Therefore, we define the diffusion length to nucleation $\lambda_N = \sqrt{D\tau_N}$ as the average travel distance of adsorbed molecules before they participate in a nucleation event at average time τ_N. After τ_N, the observable $\overline{N}$ is fully defined and the system enters the diffusion-limited aggregation (DLA) regime where growing clusters capture adsorbed diffusing molecules and locally lower $n_1(x, y, t)$. In that regime, Equation (1) is no longer suited to describe n_1.

We numerically solve Eq. (1) to find $n_1(x, y, \tau_N)$ by fixing t to τ_N and using D, R_0 and a as input parameters. The values chosen for τ_N and D are discussed below. In the early stage and complete condensation regime considered here, n_1 linearly increases with t.[24] To verify this condition, we use realistic parameters to plot the molecular concentration in the middle of the aperture $n_1(0, 0, t)$ and at the edge $n_1(-a/2, 0, t)$ as a function of $t \leq \tau_N$ for different a (see Fig. S3 in the Supporting Information). Although slight deviations from the linear behavior are observed for apertures below $a = 5$ µm, the saturation of n_1, that is characteristic of steady state, is far from achieved in this timescale. In consequence, the time derivative of $n_1(x, y, \tau_N)$ is a reasonable estimate of the local deposition flux $R(x, y)$. Next, the local nucleation density $N(x, y)$ at τ_N is obtained from the power law $N \sim R^{\delta}$ [24] and normalized to the experimental unaffected nucleation density $N_0 = 1.83 \pm 0.01$ µm^{-2} (see Fig. 5b). In the complete condensation regime, pentacene molecules on SiO_2 have a $\delta = 0.6$.[23] In a final step, $\bar{N}$ is obtained by integrating $N(x, y)$ over the aperture area and dividing by a^2.

Solving Eq. (1) requires input parameters D and τ_N that are a priori unknown. The diffusion coefficients of large organic adsorbates vary over many orders of magnitude, depending on the material system and temperature considered.[22] τ_N remains essentially unknown but is expected to be short in comparison to the timescale of the DLA regime.[25] Besides, D and τ_N are highly correlated in Eq. (1) barring their use as unambiguous fitting parameters. This ambiguity, however, can be lifted by using $\lambda_N = \sqrt{D\tau_N}$ as a single fitting parameter. This is possible because $\bar{N}$ and λ_N are directly correlated. This is shown in Figure 6a where $\bar{N}$, calculated by the numerical procedure above, is plotted as a function of realistic values of D and τ_N. The overlaid iso-λ_N lines precisely follow the contour lines of $\overline{N}$. In consequence, although the exact value of (D, τ_N) remains unknown, one can extract one λ_N corresponding to the observed $\overline{N}$.

Figure 6. a) Contour plots of the numerically simulated average nucleation density $\overline{N}$ as a function of the diffusion coefficient D and time to nucleation τ_N in a square aperture of lateral size a = 10 µm. The solid lines are contours of constant diffusion length to nucleation λ_N. b) Normalized $\overline{N}/N_0$ as a function of a/λ_N. The solid line is a fit using an empirical error function. The simulation parameters are λ_N = 0.05...1.5 µm, a = 0.1...10 µm.

The relationship between $\overline{N}$ and λ_N is further revealed in Fig. 6b: The values of $\overline{N}/N_0$, numerically simulated for different a and λ_N, all fall onto the same curve when plotted as a function of a/λ_N. A simple error function can be used as the empirical equation to represent the simulated data points:

$$\frac{\overline{N}}{N_0} = \frac{1}{2}\left[1 + \mathrm{erf}\left(\ln\left(\left(\frac{a}{A\cdot\lambda_N}\right)^B\right)\right)\right] \tag{2}$$

The best fit is obtained for parameters A = 2.505 ± 0.015, B = 0.590 ± 0.004. Using Eq. (2) with these A and B, we fit the experimental values of $\overline{N}$ in Fig. 5a using λ_N as a single fitting parameter. The best fit is obtained for λ_N = 0.66 ± 0.11 µm. This diffusion length is in the range of the value reported in the literature X_S = 2.5 µm for pentacene on SiO_2 at 40°C.[26] X_S was deduced from the inter-island distance of pentacene submonolayers grown in the complete condensation regime. X_S is defined in the DLA regime as the mean diffusion length of molecules before desorption. In this regime, conditions for nucleation are no longer met in the inter-grain region and individual molecular adsorbates can diffuse over distances $X_S > \lambda_N$ before desorption. In conclusion of the modeling, our numerical model is condensed into Eq. (2) that captures well the experimental trend. This formula, parameterized with values found for A and B, is useful to experimentalists who want to fit experimental data obtained with square stencil apertures without developing a complex numerical model. A mathematically-derived analytical formulation linking $\bar{N}/N_0$ to a/λ_N is desirable to obtain more physical insights into the diffusion dynamics. This derivation over a two dimensional square case is however complex and left to further work.

The diffusion of adsorbed molecules under the stencil mask also explains the cross-talk between neighboring apertures observed for short inter-aperture distance d in Fig. 3. When d approaches λ_N, the 2D gas of adsorbed molecules with non-negligible concentration n_1 bridges the unexposed space between apertures. In this case, since the molecular diffusion flux from the aperture to the unexposed area is proportional to the gradient of n_1, diffusion is decreased. Consequently, n_1 is higher in the apertures and nucleation becomes more probable. This explains the presence of homogeneously nucleated grains even for the smallest a = 0.5 μm in Fig. 3d. Also, at $d \sim \lambda_N$, molecules originating from one aperture may feed a stable cluster formed in a neighboring aperture. Upon further growth, this may yield monolayer grains encompassing several apertures (see Fig. 3d).

Finally, the growth of the large single-crystalline pentacene monolayer islands observed for a = 1 μm ~ $2\lambda_N$ and d = 5 μm >> λ_N in Figs. 1f and 2 is quite extraordinary. Their elliptical shape corresponds to the equilibrium crystal shape of pentacene smoothed out by the diffusive supply of adsorbed molecules. The VTE growth conditions are highly out-of-equilibrium and usually result in morphologies dominated by kinetic processes such as dendritic growth observed in Fig. 1c. Producing an equilibrium shape in such conditions is only made possible by the diffusion-mediated slow supply of molecules to the advancing step edge. Furthermore, this unusual growth reveals that the homogeneous nucleation of the second monolayer in the aperture area is discouraged. Several causes can lie at the origin of this: the absence of grain boundaries in the first monolayer offer few sites for nucleation (high $\Delta\mu_{\mathrm{cr}}$ on the surface of the crystalline grain), high diffusivity of pentacene on pentacene (long λ_{D}), limited reflection of the diffusing molecules on the growing step edge (low Ehlrich-Schwoebel barrier for the crossing of the grain step edge by the diffusing molecules).[27] The precise understanding and quantification of this growth behavior requires specialized modeling tools such as kinetic Monte-Carlo simulations that combine all of the microscopic events described above.[28,29] This is left to further work. For large apertures of a = 10 µm, this diffusion-driven growth is not observed. In this case, multiple grain boundaries suppress molecular diffusion and act as nucleation sites for subsequent layers restricting the film to the aperture area.

The pentacene single crystal arrays shown in Fig. 2 could find application as the active layer of high performance TFT arrays for circuit applications. Due to anisotropy of transport properties, the random crystal orientation on the substrate observed in Fig. 2 would however result in a spread of electrical characteristics, thereby barring multiple device integration. In order to control grain orientation, the surface energy of the substrate can be patterned to promote film growth along one direction. This strategy has been demonstrated by limiting the growth area using line patterns of fluorinated polymers or self-assembled monolayers.[30] The bounded crystals can then reorient during growth along the patterned direction. In this approach, the alignment of stencil mask apertures to the patterned areas remains a technical challenge that is left to further work. More generally, the use of surface treatments and metallization layers in combination with patterning techniques necessary for the fabrication of TFT arrays could be employed to control both nucleation and crystal orientation. This requires an in-depth understanding of the diffusion and nucleation phenomena discussed in this paper.

Conclusions

In this work, we described the stencil evaporation method for the growth of dense arrays of single crystalline pentacene grains. Stencil evaporation consists in the use of a micro-structured shadow mask to locally define where an organic semiconductor grows on a surface. This method is scalable down to sub-micrometer scale and is well adapted to vacuum thermal evaporation in standard equipment. We show that this technique provides an additional parameter for locally controlling the film growth through the surface diffusion of adsorbed molecules. The numerical analysis of the nucleation density measured in apertures of decreasing sizes leads to the extraction of the molecular diffusion length before nucleation λ_N. We estimate $\lambda_N = 0.66 \pm 0.11$ µm for the diffusion of pentacene on SiO_2 at the substrate temperature of 40°C, that is in the range of literature values. Additionally, optimal conditions for nucleation of single grains per aperture are obtained when the aperture size is in the range of $2\lambda_N$ and when the distance between neighboring apertures is substantially larger than λ_N.

Upon further growth in the apertures where single grains nucleated, elliptically shaped monolayer islands are formed with lateral dimensions that are several times the aperture size. Transverse shear microscopy and differential interference contrast both show that these islands are single crystals. Their elliptical shape is reminiscent of the crystal habit of pentacene smoothed out by the supply of diffusive molecules. Deciphering the microscopic events underlying this extraordinary growth would offer important insights in the formation of thin crystalline films of organic semiconductors from the vapor phase.

In conclusion, we demonstrated stencil lithography, a method that opens new possibilities for experimental organic crystal growth studies and that ultimately enables the fabrication of dense arrays of thin-film single crystals of organic semiconductors.

Experimental section

Thermally grown SiO_2 (thickness ≈ 120 nm) was used as a substrate for the film deposition. Prior to the deposition, the substrates were cleaned with acetone in the ultrasonic bath in order to degrease and remove particles left after wafer dicing. Then acetone was rinsed away with isopropyl alcohol (IPA) followed by drying with nitrogen gas.

The surface energy of SiO_2 was calculated from static contact angle measurements using optical contact angle measurement system Dataphysics OCA20LH. Two probe liquids water and glycerol resulted in contact angles $\theta = 41.0° \pm 2.3°$ and $\theta = 27.8° \pm 1.9°$ respectively. The surface tensions for probe liquids were taken from Ref. [31] According to the Owens/Wendt theory, the total surface energy is $\gamma = 57.8$ mJ/m^2 with dispersive $\gamma^D = 27.8$ mJ/m^2 and polar $\gamma^P = 30.0$ mJ/m^2 components. Our values are in good agreement with previously published results that used similar cleaning procedures.[23]

The surface roughness of the SiO_2 substrate was measured by the AFM system Bruker Dimension Edge. Its RMS roughness value of 2.1 Å is comparable to the previously published results (2.1 Å ± 0.1 Å) that used the same cleaning procedure.[23]

Stencils were fabricated via the patterning and subsequent release of low stress silicon nitride membranes. A 50 nm thick, sputtered silicon hard mask was patterned via electron beam lithography and dry etching. The apertures, down to 200 nm, etched in the hard mask were transferred through a second dry etching step to the underlying low-stress, 200 nm thick, silicon rich nitride film. Following this front side patterning, the silicon nitride layer was protected with Protek B3 polymer to preserve fragile nanoaperture grids during the full wafer KOH backside etch used to release the membrane from the silicon substrate. More details on stencil fabrication can be found elsewhere.[32] In order to remove pentacene from previous depositions, stencils were immersed in 1,2,4-trichlorobenzene at 70°C for 10 minutes, followed by IPA rinse and dried on a hot plate. Stencil masks were taped to the middle of the sample and removed after the deposition.

Pentacene (purchased from Sigma-Aldrich) was purified once by physical vapor transport before loading in the deposition chamber. Pentacene film deposition was done by thermal evaporation in high vacuum (10^{-7} torr) using the Kurt J. Lesker Super Spectros tool. The deposition rate and film thickness were controlled by quartz crystal monitor (QCM) kept at 20°C. Substrates were preheated inside the vacuum chamber for one hour prior the deposition to reach the desired temperature. Both QCM and the substrate heater were carefully calibrated prior the deposition.

Imaging of pentacene submonolayers was done using SEM Philips XL30 with in-lens detector for secondary electrons, in the immersion mode, at the tension of 3 kV. Due to the low density of organic materials, incident high-energy electron beam penetrates pentacene film without significant generation of secondary electrons. When the beam reaches high-density SiO_2, incident electrons undergo multiple scattering events and generate large number of secondary electrons. However, due to low energy of secondary electrons (10-50 eV), their escape depth is very small (1-2 nm)[33] and most of them are scattered by the overlaying pentacene islands. Consequently, this results in dark areas on the SEM image and from obtained contrast, pentacene nucleation density can be calculated. Although AFM is typically used for this purpose, it is impractical to locate micro patterned submonolayer films that are invisible in the AFM optical system. On the contrary, SEM allows real-time visualization and fast image acquisition, however, at the expense of lower contrast. More detailed comparison of AFM and SEM as calculation techniques for the nucleation density can be found in the Supporting Information (Fig. S1). The nucleation density was calculated from obtained SEM pictures using Mathematica computational software. To obtain statistics, three SEM images were taken for each aperture size. Numerical modeling of the nucleation density was done using COMSOL.

TSM images were taken in the contact mode using the AFM system Bruker Dimension Edge. Silicon nitride V-shaped probes Bruker SNL (nominal resonant frequency 65 kHz, spring constant 0.35 N/m) were used for the TSM measurements. Due to the absence of environmental chamber for the AFM, the relative humidity was around 40%.

DIC images were taken in the reflection configuration using the optical microscope Olympus AX70.

Supporting Information

The Supporting Information is available free of charge:

> Additional figures that compare the nucleation density N calculated by SEM and AFM; that describe calculation procedure for the unaffected nucleation density N_0; that show time evolution of the molecular concentration in the center $n_1(0, 0, t)$ and at the edge of the aperture $n_1(-a/2, 0, t)$.

Acknowledgments

The research leading to these results has received funding from the European Research Council under the European Union's Seventh Framework Programme (FP7/2007-2013) / ERC grant agreement n°320680 (EPOS CRYSTALLI).

References

(1) Zschieschang, U.; Kang, M. J.; Takimiya, K.; Sekitani, T.; Someya, T.; Canzler, T. W.;

Werner, A.; Blochwitz-Nimoth, J.; Klauk, H. Flexible Low-Voltage Organic Thin-Film Transistors and Circuits Based on C10-DNTT. *J. Mater. Chem.* **2012**, *22*, 4273.

(2) Yokota, T.; Kuribara, K.; Tokuhara, T.; Zschieschang, U.; Klauk, H.; Takimiya, K.; Sadamitsu, Y.; Hamada, M.; Sekitani, T.; Someya, T. Flexible Low-Voltage Organic Transistors with High Thermal Stability at 250 °C. *Adv. Mater.* **2013**, *25*, 3639–3644.

(3) Forrest, S. R. The Path to Ubiquitous and Low-Cost Organic Electronic Appliances on Plastic. *Nature* **2004**, *428*, 911–918.

(4) Søndergaard, R. R.; Hösel, M.; Krebs, F. C. Roll-to-Roll Fabrication of Large Area Functional Organic Materials. *J. Polym. Sci. Part B Polym. Phys.* **2013**, *51*, 16–34.

(5) Kelley, T. W.; Frisbie, C. D. Gate Voltage Dependent Resistance of a Single Organic Semiconductor Grain Boundary. *J. Phys. Chem. B* **2001**, *105*, 4538–4540.

(6) Lunt, R. R.; Benziger, J. B.; Forrest, S. R. Relationship between Crystalline Order and Exciton Diffusion Length in Molecular Organic Semiconductors. *Adv. Mater.* **2010**, *22*, 1233–1236.

(7) Lee, S. S.; Kim, C. S.; Gomez, E. D.; Purushothaman, B.; Toney, M. F.; Wang, C.; Hexemer, A.; Anthony, J. E.; Loo, Y. L. Controlling Nucleation and Crystallization in Solution-Processed Organic Semiconductors for Thin-Film Transistors. *Adv. Mater.* **2009**, *21*, 3605–3609.

(8) De Vusser, S.; Steudel, S.; Myny, K.; Genoe, J.; Heremans, P. Integrated Shadow Mask Method for Patterning Small Molecule Organic Semiconductors. *Appl. Phys. Lett.* **2006**, *88*, 2004–2007.

(9) Briseno, A. L.; Mannsfeld, S. C. B.; Ling, M. M.; Liu, S.; Tseng, R. J.; Reese, C.; Roberts, M. E.; Yang, Y.; Wudl, F.; Bao, Z. Patterning Organic Single-Crystal Transistor Arrays. *Nature* **2006**, *444*, 913–917.

(10) Minemawari, H.; Yamada, T.; Matsui, H.; Tsutsumi, J.; Haas, S.; Chiba, R.; Kumai, R.; Hasegawa, T. Inkjet Printing of Single-Crystal Films. *Nature* **2011**, *475*, 364–367.

(11) Nakayama, K.; Hirose, Y.; Soeda, J.; Yoshizumi, M.; Uemura, T.; Uno, M.; Li, W.; Kang, M. J.; Yamagishi, M.; Okada, Y.; *et al.* Patternable Solution-Crystallized Organic Transistors with High Charge Carrier Mobility. *Adv. Mater.* **2011**, *23*, 1626–1629.

(12) Diao, Y.; Tee, B. C.-K.; Giri, G.; Xu, J.; Kim, D. H.; Becerril, H. a; Stoltenberg, R. M.; Lee, T. H.; Xue, G.; Mannsfeld, S. C. B.; *et al.* Solution Coating of Large-Area Organic Semiconductor Thin Films with Aligned Single-Crystalline Domains. *Nat. Mater.* **2013**, *12*, 665–671.

(13) Laudise, R. .; Kloc, C.; Simpkins, P. .; Siegrist, T. Physical Vapor Growth of Organic Semiconductors. *J. Cryst. Growth* **1998**, *187*, 449–454.

(14) Sidler, K.; Cvetkovic, N. V.; Savu, V.; Tsamados, D.; Ionescu, A. M.; Brugger, J. Organic Thin Film Transistors on Flexible Polyimide Substrates Fabricated by Full-Wafer Stencil Lithography. *Sensors Actuators, A Phys.* **2010**, *162*, 155–159.

(15) Ruiz, R.; Choudhary, D.; Nickel, B.; Toccoli, T.; Chang, K.-C.; Mayer, A. C.; Clancy, P.; Blakely, J. M.; Headrick, R. L.; Iannotta, S.; *et al.* Pentacene Thin Film Growth. *Chem. Mater.* **2004**, *16*, 4497–4508.

(16) Kalihari, V.; Tadmor, E. B.; Haugstad, G.; Frisbie, C. D. Grain Orientation Mapping of

Polycrystalline Organic Semiconductor Films by Transverse Shear Microscopy. *Adv. Mater.* **2008**, *20*, 4033–4039.

(17) Fesenko, P.; Rolin, C.; Janneck, R.; Bommanaboyena, S. P.; Gaethje, H.; Heremans, P.; Genoe, J. Determination of Crystal Orientation in Organic Thin Films Using Optical Microscopy. *Org. Electron.* **2016**, 10.1016/j.orgel.2016.06.011.

(18) Faltermeier, D.; Gompf, B.; Dressel, M.; Tripathi, A. K.; Pflaum, J. Optical Properties of Pentacene Thin Films and Single Crystals. *Phys. Rev. B - Condens. Matter Mater. Phys.* **2006**, *74*, 1–6.

(19) Verlaak, S.; Steudel, S.; Heremans, P.; Janssen, D.; Deleuze, M. Nucleation of Organic Semiconductors on Inert Substrates. *Phys. Rev. B* **2003**, *68*, 195409.

(20) Mutaftschiev, B. *The Atomistic Nature of Crystal Growth*; Springer Series in Materials Science; Springer Berlin Heidelberg: Berlin, Heidelberg, 2001; Vol. 43.

(21) Mannsfeld, S. C. B.; Briseno, A. L.; Liu, S.; Reese, C.; Roberts, M. E.; Bao, Z. Selective Nucleation of Organic Single Crystals from Vapor Phase on Nanoscopically Rough Surfaces. *Adv. Funct. Mater.* **2007**, *17*, 3545–3553.

(22) Barth, J. V. Transport of Adsorbates at Metal Surfaces: From Thermal Migration to Hot Precursors. *Surf. Sci. Rep.* **2000**, *40*, 75–149.

(23) Ribič, P.; Kalihari, V.; Frisbie, C.; Bratina, G. Growth of Ultrathin Pentacene Films on Polymeric Substrates. *Phys. Rev. B* **2009**, *80*, 115307.

(24) Venables, J. A.; Spiller, G. D. T.; Hanbucken, M. Nucleation and Growth of Thin Films. *Reports Prog. Phys.* **1984**, *47*, 399–459.

(25) Meyer zu Heringdorf, F. J.; Reuter, M. C.; Tromp, R. M. Growth Dynamics of Pentacene Thin Films. *Nature* **2001**, *412*, 517–520.

(26) Stadlober, B.; Haas, U.; Maresch, H.; Haase, A. Growth Model of Pentacene on Inorganic and Organic Dielectrics Based on Scaling and Rate-Equation Theory. *Phys. Rev. B* **2006**, *74*, 165302.

(27) Goose, J. E.; First, E. L.; Clancy, P. Nature of Step-Edge Barriers for Small Organic Molecules. *Phys. Rev. B - Condens. Matter Mater. Phys.* **2010**, *81*, 10–12.

(28) Bommel, S.; Kleppmann, N.; Weber, C.; Spranger, H.; Schäfer, P.; Novak, J.; Roth, S. V.; Schreiber, F.; Klapp, S. H. L.; Kowarik, S. Unravelling the Multilayer Growth of the Fullerene C60 in Real Time. *Nat. Commun.* **2014**, *5*, 5388.

(29) Choudhary, D.; Clancy, P.; Shetty, R.; Escobedo, F. A Computational Study of the Sub-Monolayer Growth of Pentacene. *Adv. Funct. Mater.* **2006**, *16*, 1768–1775.

(30) Kumatani, A.; Liu, C.; Li, Y.; Darmawan, P.; Takimiya, K.; Minari, T.; Tsukagoshi, K. Solution-Processed, Self-Organized Organic Single Crystal Arrays with Controlled Crystal Orientation. *Sci. Rep.* **2012**, *2*, 393.

(31) Wu, S. *Polymer Interface and Adhesion*; CRC Press, 1982.

(32) Villanueva, G.; Vazquez-Mena, O.; van den Boogaart, M. A. F.; Sidler, K.; Pataky, K.; Savu, V.; Brugger, J. Etching of Sub-Micrometer Structures through Stencil. *Microelectron. Eng.* **2008**, *85*, 1010–1014.

(33) Brandon, D. G.; Kaplan, W. D. *Microstructural Characterization of Materials*; John Wiley, 2008.

For Table of Contents Use Only

Manuscript title: Arrays of pentacene single crystals by stencil evaporation

Author list: Pavlo Fesenko, Valentin Flauraud, Shenqi Xie, Jürgen Brugger, Jan Genoe, Paul Heremans, Cédric Rolin

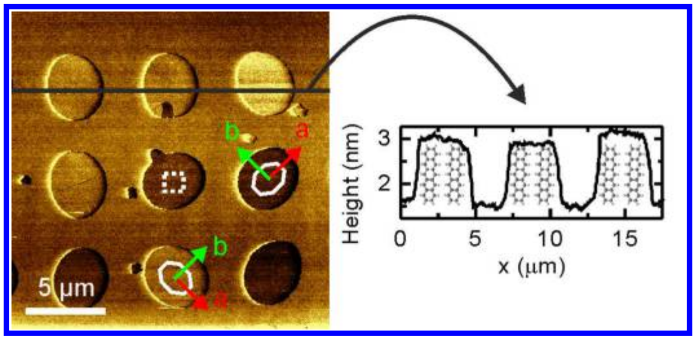

Synopsis: Arrays of pentacene single crystals are patterned on SiO_2 substrates by stencil evaporation, a technique that combines micro-fabricated stencils with vacuum evaporation in standard conditions. Using micron scale apertures enables a control over nucleation and subsequent diffusive growth. A model is proposed to extract the molecular diffusion length.

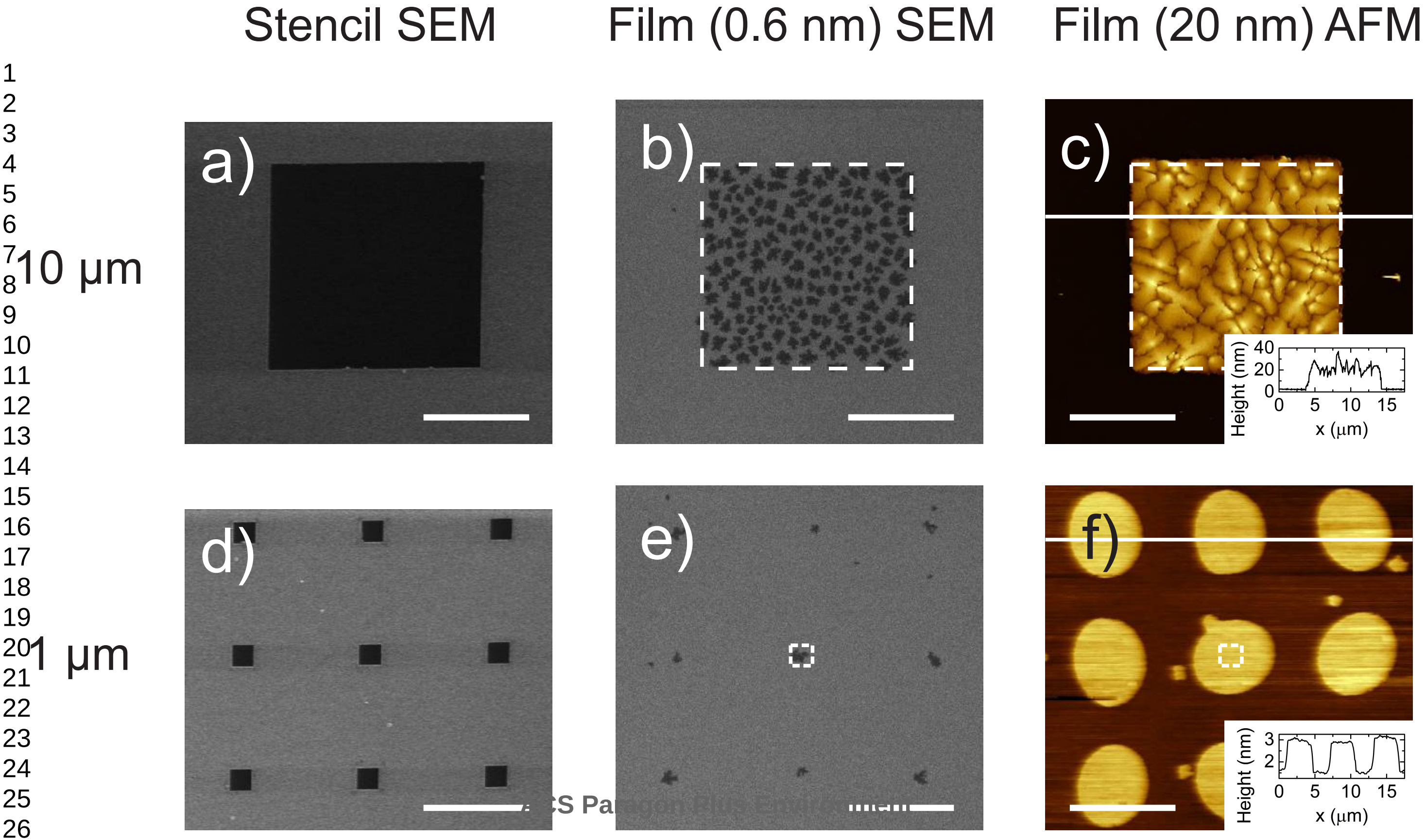
Stencil SEM
Film (0.6 nm) SEM
Film (20 nm) AFM
10 µm
1 µm
a)
b)
c)
d)
e)
f)
Height (nm)
40
20
0
0
5
10
15
x (µm)
Height (nm)
3
2
0
5
10
15
x (µm)

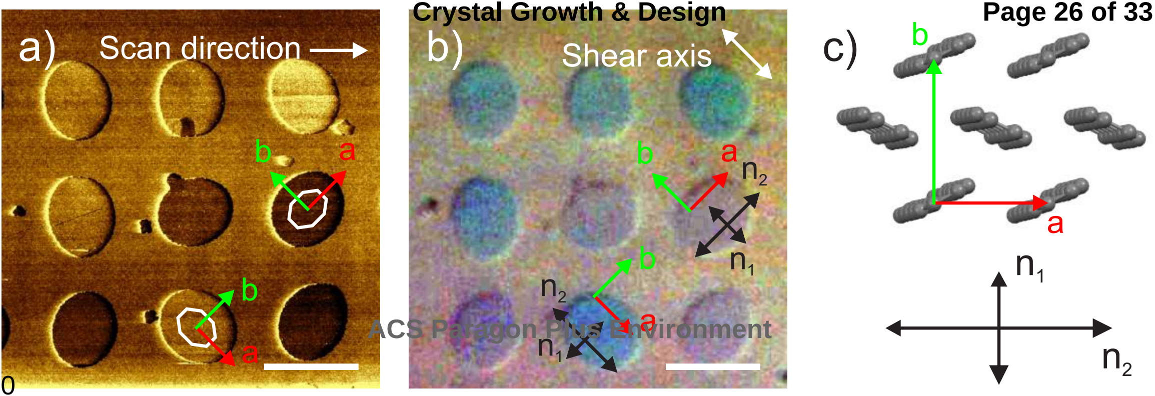
a)
Scan direction
b
a
b
a
b)
Shear axis
b
a
n_2
n_1
b
n_2
a
n_1
c)
b
a
n_1
n_2

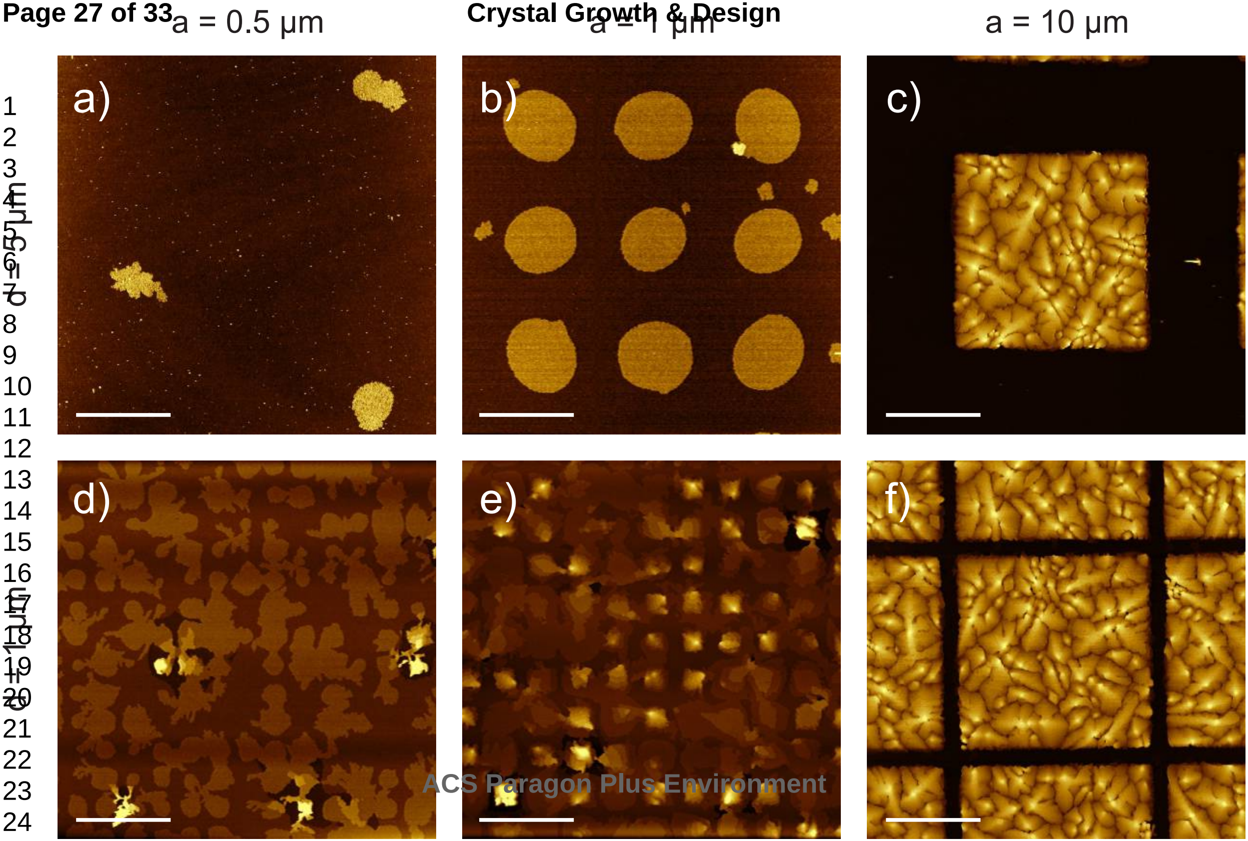
a = 0.5 µm
a = 1 µm
a = 10 µm
d = 5 µm
d = 1 µm
a)
b)
c)
d)
e)
f)

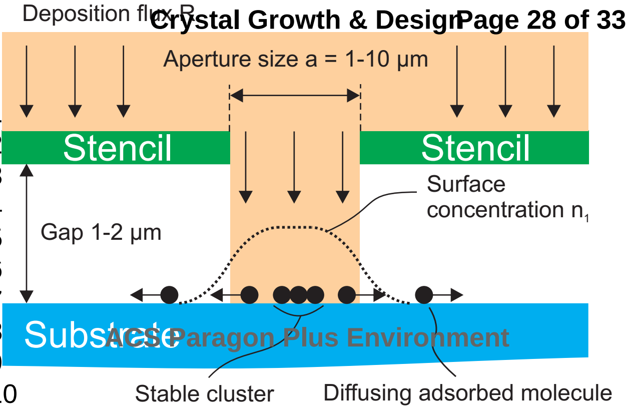
Deposition flux R
Aperture size a = 1-10 μm
Stencil
Stencil
Surface concentration n₁
Gap 1-2 μm
Substrate
Stable cluster
Diffusing adsorbed molecule

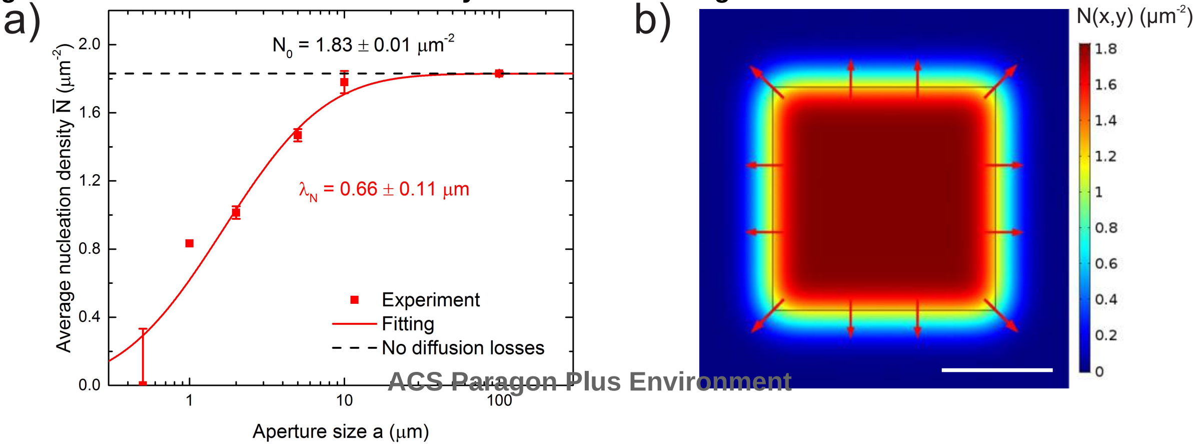
a)
Average nucleation density $\overline{N}$ (μm^{-2})
2.0
1.6
1.2
0.8
0.4
0.0
N_0 = 1.83 ± 0.01 μm^{-2}
λ_N = 0.66 ± 0.11 μm
Experiment
Fitting
No diffusion losses
1
10
100
Aperture size a (μm)
b)
N(x,y) (μm^{-2})
1.8
1.6
1.4
1.2
1
0.8
0.6
0.4
0.2
0

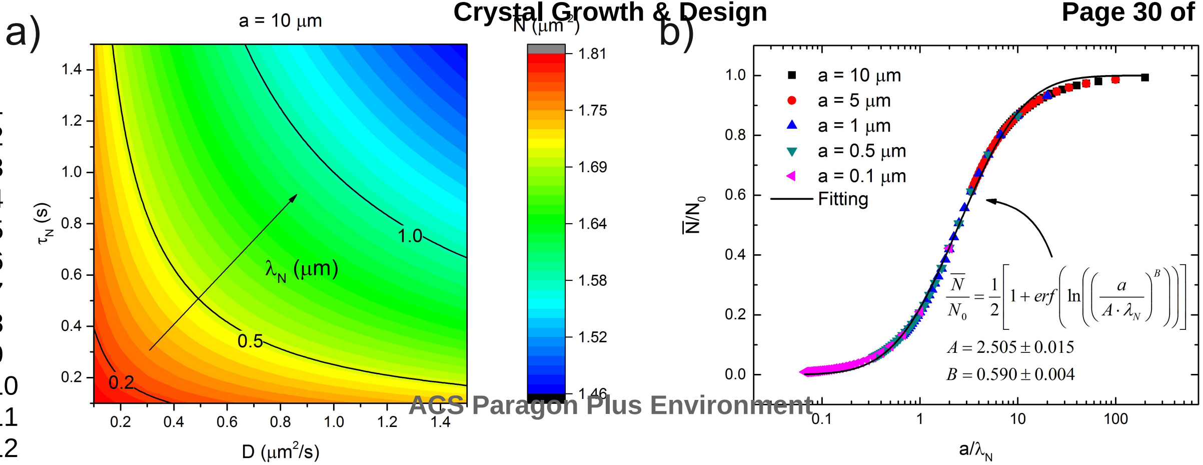
a)
a = 10 µm
$\bar{N}$ (µm^{-2})
1.81
1.75
1.69
1.64
1.58
1.52
1.46
τ_N (s)
1.4
1.2
1.0
0.8
0.6
0.4
0.2
D (µm^2/s)
0.2
0.4
0.6
0.8
1.0
1.2
1.4
λ_N (µm)
1.0
0.5
0.2
b)
$\overline{N}/N_0$
1.0
0.8
0.6
0.4
0.2
0.0
a = 10 µm
a = 5 µm
a = 1 µm
a = 0.5 µm
a = 0.1 µm
Fitting
$\frac{\overline{N}}{N_0} = \frac{1}{2}\left[1 + erf\left(\ln\left(\left(\frac{a}{A \cdot \lambda_N}\right)^B\right)\right)\right]$
$A = 2.505 \pm 0.015$
$B = 0.590 \pm 0.004$
0.1
1
10
100
a/λ_N

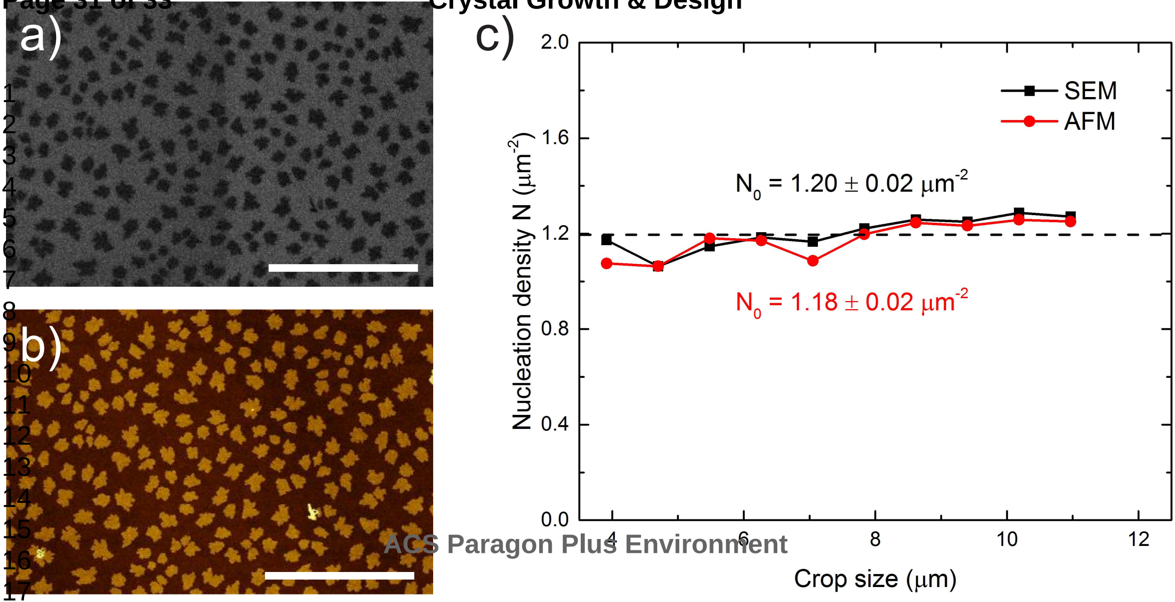
a)
b)
c)
Nucleation density N (μm^{-2})
Crop size (μm)
SEM
AFM
$N_0 = 1.20 \pm 0.02\ \mu m^{-2}$
$N_0 = 1.18 \pm 0.02\ \mu m^{-2}$
2.0
1.6
1.2
0.8
0.4
0.0
4
6
8
10
12

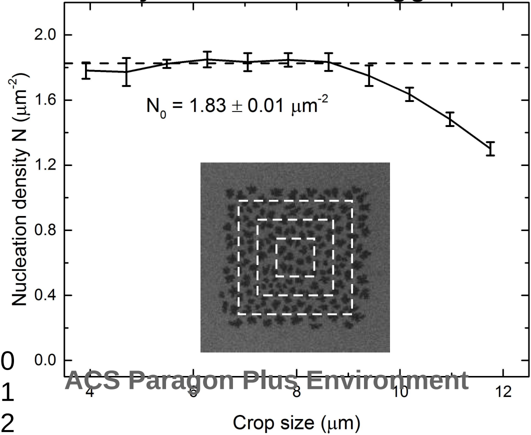
Nucleation density N (μm^{-2})
2.0
1.6
1.2
0.8
0.4
0.0
$N_0 = 1.83 \pm 0.01\ \mu m^{-2}$
4
6
8
10
12
Crop size (μm)

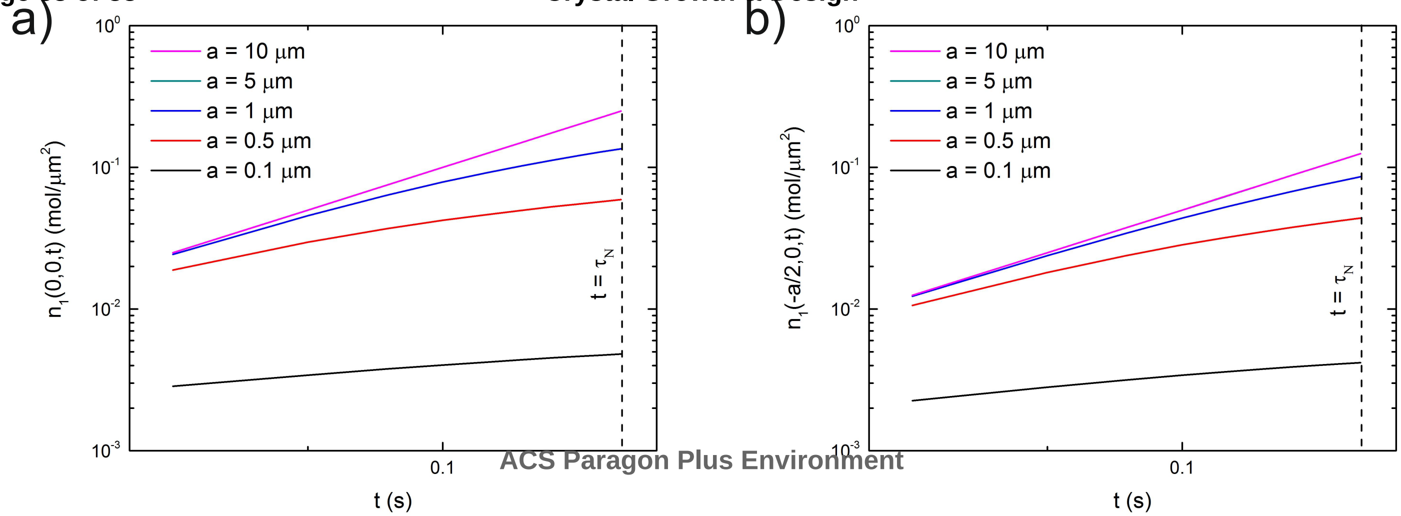
a)
10^0
10^{-1}
10^{-2}
10^{-3}
$n_1(0,0,t)$ (mol/μm^2)
a = 10 μm
a = 5 μm
a = 1 μm
a = 0.5 μm
a = 0.1 μm
$t = \tau_N$
0.1
t (s)
b)
10^0
10^{-1}
10^{-2}
10^{-3}
$n_1(-a/2,0,t)$ (mol/μm^2)
a = 10 μm
a = 5 μm
a = 1 μm
a = 0.5 μm
a = 0.1 μm
$t = \tau_N$
0.1
t (s)